On Extracting Subfemtosecond Data from Femtosecond Quantum Dynamics Calculations: The Methane Cation

T. Mondal[†,‡] and A. J. C. Varandas*[,†]

[†]Departamento de Química, and Centro de Química, Universidade de Coimbra, 3004-535 Coimbra, Portugal
[‡]Department of Chemistry, Birla Institute of Technology & Science, Pilani - K.K. Birla Goa Campus, Goa 403 726, India

ABSTRACT: Motivated by recent measurements of the subfemtosecond structural rearrangement in the methane cation using high-harmonic generation technology, here, we attempt an *ab initio* quantum dynamics study to explore such an event by modeling the experiments. This is done by calculating the ratio of the squared autocorrelation functions of wave packets that evolve on the $\tilde{X}^2T_2$ electronic manifold of the isotopes CD_4^+ and CH_4^+, in full dimensionality including nonadiabatic coupling. We have found good agreement with the experimental data, and additionally predict an unexpected maximum in the above ratio at ∼1.85 fs, thence outside the experimentally covered time-delay window. We further predict the above structural rearrangements to occur in ∼1.85 fs, and we propose a mechanism for this via a five-dimensional hypersurface developed from the JT active bending vibrations of e and t_2 symmetry. Recurrences of such a maximum are also found with an interval of time delays, and the average of such intervals suggested corroboration of the oscillation time between the T_d and the C_{2v} geometries of CH_4^+. Furthermore, we perform a dynamics study up to 200 fs, and we unravel the underlying details of the first photoelectron band of CD_4.
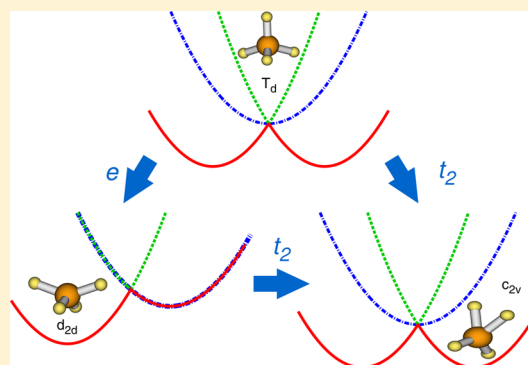
1. INTRODUCTION

Imaging structures and dynamics is a major direction of modern science which encompasses physics, chemistry, and biology. Accordingly, the study of nuclear dynamics and structural rearrangement on the molecular time scale has become possible with the advent of femtosecond science, which uses laser pulses to excite molecules and delayed pulses to interrogate the time evolution of the excited species (the so-called "pump−probe method"). Currently, great interest in the development of methods to probe nuclear dynamics with attosecond resolution ($10^{-18}-10^{-15}$ s) has emerged.[1−4] The leading approach is the generation of attosecond pulses by ionizing atoms with intense laser pulses, which leads to the production of high-order harmonics from molecules. This high-harmonic generation (HHG) can be understood within the framework of a semiclassical "three-step" model.[5,6] In the first step, an intense laser pulse ionizes an atom or molecule, launching a correlated electronic and vibrational wave packet (WP) pair. In the next step, the vibrational WP moves on the ground-state potential energy surface (PES) of the ionic species, while the electron WP moves in response to the laser electric field. In this step, the electron WP is first accelerated away from the parent ion and then driven back as the laser field reverses its direction. The third step is the recombination of the recolliding electron with the parent ion and the emission of a high-energy photon (∼10−500 eV), i.e., HHG.[5,7] Thus, the attosecond pulse could be produced by making an inverse Fourier transformation of the emitted harmonics.[8,9] The intensity of such harmonic radiation depends on the transition amplitude between the wave function describing the electron and ion at that moment and the wave function of the initial molecular ground state. As a result, the emitted high harmonic radiation is sensitive to small changes in the molecular geometry occurring within a fraction of the vibrational period. Therefore, the effect of nuclear motion on HHG spectroscopy can be incorporated through the nuclear autocorrelation function, which describes the nuclear WP dynamics in the molecular cation from the time of ionization to the moment of recollision. In other words, the details of the nuclear dynamics must be encoded in the HHG signal. Approximately, the HHG signal is proportional to the squared modulus of the nuclear autocorrelation function.[10] Such a formulation is turned into a popular method for imaging ultrafast nuclear dynamics by taking the ratio of HHG spectra of the two isotopes, the so-called "PACER" (Probing Attosecond dynamics with Chirped Encoded Recollisions).[4,10]

Since the mapping of the above harmonic order is only possible up to ∼1.6 fs at a wavelength of 800 nm, only the lightest nuclei can move significantly during this period of time. Accordingly, the nuclear motion within such a time scale has been investigated[4,11] for the lightest molecules of H_2 and D_2, and CH_4 and CD_4. Surprisingly, a more pronounced isotopic effect and faster nuclear dynamics have been observed[4] for CD_4/CH_4 than D_2/H_2, despite the former being considerably heavier than the latter, with slower nuclei therefore involved. In

turn, Chirilă and Lein[12] have calculated the ratio of the harmonic intensities in D_2/H_2 with a somewhat improved theoretical model by considering the "vibrational correlation function". Three years later, Patchkoviskii[13] explained the above surprisingly fast nuclear dynamics of CD_4/CH_4 based on the increasing change of the PES upon ionization when going from CD_4/CH_4 to D/H_2. Such a result has been obtained using normal-mode coordinates and both gradient and curvature terms of the CD_4^+/CH_4^+ PESs (which were estimated to be larger than for D_2^+/H_2^+), with the change in curvature accounting for the fastness of the nuclear dynamics (the decay rate of the nuclear autocorrelation function). In fact, its important role had already been pointed out[14] for strong-field ionization of molecules, and the consequences for a laser-induced nuclear dynamics have been discussed.[15] The large changes in the curvature of the PES of ionic species is particularly true for Jahn–Teller (JT) cations. Indeed, the ionization of an electron from the highest occupied molecular orbital of the equilibrium configuration of CH_4 (T_d) yields CH_4^+ in its ground state ($\tilde{X}^2T_2$), which is known to undergo JT distortion. Accordingly, the three-fold degeneracy of the ground electronic state of the cation is split into three nondegenerate electronic states. Thus, the JT effect plays a pivotal role on the nuclear dynamics. Patchkoviskii[13] did not explicitly account for the JT effect when calculating the gradient and curvature of the ground electronic state of the cation. Instead, he has applied various arbitrary static electric fields to capture the splitting of the electronic degeneracy. Therefore, it should be emphasized that the present study explicitly accounts for the JT effect within a quadratic vibronic coupling (QVC) scheme, with the ratio of the squared modulus of the autocorrelation functions of CD_4^+/CH_4^+ recalculated in the full 9D vibrational space. In addition, we report a comparison with the available experimental observations.[4]

In a recent study of D_2O/H_2O,[16] it has also been established that the difference of potentials between neutral and ground electronic state determines the speed of the nuclear dynamics of the cation. Although, for diatomics, the autocorrelation function can be calculated exactly,[4,10] this is not true for larger polyatomics, where an exact treatment is prohibitively expensive. In this case, it may alternatively be extracted from experimental photoelectron spectra.[16] Such a procedure has been utilized for ND_3/NH_3,[17] accompanied by theoretical work adopting a 1D model.[18] However, in strong-field ionization, the transition amplitude due to one-photon ionization shows pronounced deviations from the Franck–Condon approximation. A way to estimate the correct autocorrelation function has recently been proposed.[17] Naturally, in contrast to quantum calculations, the extraction of the autocorrelation function from experimental spectra may provide accurate data in full dimensionality for any size of molecule. Indeed, apart from the strong field correction, the extracted autocorrelation function will be exact within the experimental accuracy of the photoelectron spectra. However, one disadvantage is that the autocorrelation function so extracted, and, hence, the nuclear motion measured in HHG experiments, cannot be easily inverted to explore the WP dynamics, which is the original goal of such experiments.[18]

The goal of the present article is to explore the subfemtosecond nuclear dynamics of the triply degenerate ground electronic manifold ($\tilde{X}^2T_2$) of CH_4^+ by simulating the dynamical observables of the HHG spectroscopy. This is done by calculating the nuclear autocorrelation functions for both CH_4^+ and CD_4^+, which are obtained through solution of the time-dependent Schrödinger equation. The required Hamiltonian has been adopted from our previous work[19,20] within a QVC scheme. Multireference-wave-function-based calculations are performed to establish the pertinent PESs and associated diabatic coupling elements. The full-dimensional quantum dynamics simulations are done by propagating the WPs utilizing the multiconfiguration time-dependent Hartree (MCTDH) method.[21–25] This dynamics study is performed up to 200 fs for calculating the first photoelectron band of CD_4, as the same has been accomplished for CH_4 in our previous work,[19,26] and has been used here for comparison. We then first extract our quantum dynamics results in the subfemtosecond regime (~1.6 fs) for both CH_4^+ and CD_4^+ and compare our results with recent experimental recordings of the ratio of the harmonic spectra generated in gaseous CH_4 and CD_4.[4] This will enable us to unravel the ultrafast vibrational dynamics of CH_4^+ and CD_4^+ in the subfemtosecond time scale. The use of isotopes ensures that the variation in HHG spectra is due primarily to differing nuclear dynamics, because the electronic states within a Born–Oppenheimer (BO) framework are identical. The variation of this ratio with high harmonic order then yields information concerning the differing nuclear (proton or deuteron) dynamics in the ions of the two species. Subsequently, we estimate the ratio of the square modulus of the autocorrelation function of both cationic isomers over a longer time window for examining their nuclear dynamics with much wider temporal resolution.

The paper is organized as follows. Section 2 presents a brief synopsis of the theory regarding the electronic structure and quantum dynamics calculations. Section 3 discusses the results on the calculation of the PESs and determination of various critical points on them, as well as the underlying details of the first photoelectron band of CD_4. Section 4 describes the relation of the nuclear autocorrelation function to the intensity of the HHG signal and unravel the ultrafast proton dynamics of CH_4^+ in the subfemtosecond regime. Finally, section 5 concludes the current work.

2. THEORETICAL AND COMPUTATIONAL ASPECTS

2.1. Vibronic Hamiltonian. As mentioned above, we have utilized the quadratic vibronic coupling Hamiltonian model for simulating the nuclear dynamics of ground state ($\tilde{X}^2T_2$) CH_4^+ and SiH_4^+.[19,20] Since it has been described in detail in previous papers, we summarize here for completeness only the basic equations while pointing out where modifications are done to handle CD_4^+. Similarly, the protonated cations, the $\tilde{X}^2T_2$ electronic state of CD_4^+ undergoes JT[27–34] splitting in first order due to distorting from the equilibrium configuration, $Q = 0$, of ground state CD_4 along nuclear vibrations of either e or t_2 symmetry; the totally symmetric a_1 vibrational mode is tuning active within this electronic manifold.[32] A diabatic electronic representation is then employed to set up the Hamiltonian. All the three diagonal sheets of $\tilde{X}^2T_2$ symmetry and their couplings are then expanded as a Taylor series in dimensionless normal coordinates (e.g., Q_i for vibrational mode ν_i) of the electronic ground state ($\tilde{X}^1A_1$) of CD_4, and truncated at second-order. Thus, all matrix elements are considered up to second-order of all possible nontotally symmetric tensor convolutions that can be obtained from quadratic combinations involving the e and t_2 vibrational modes.

The diabatic vibronic Hamiltonian, on the basis of dimensionless normal coordinates (Q_i) of the vibrational modes (ν_i), then assumes the form

$$\mathcal{H} = \mathcal{H}_0 1_3 + \mathcal{W} \tag{1}$$

where $\mathcal{H}_0$ is the unperturbed Hamiltonian for the electronic ground state of CD_4 ($\mathcal{H}_0 = \mathcal{T}_N + \mathcal{V}_0$) within the harmonic approximation,

$$\mathcal{T}_N = -\frac{1}{2}\omega_1\frac{\partial^2}{\partial Q_1^2} - \frac{1}{2}\omega_2\left(\frac{\partial^2}{\partial Q_{2\theta}^2} + \frac{\partial^2}{\partial Q_{2\epsilon}^2}\right)$$
$$- \frac{1}{2}\sum_{i=3}^{4}\omega_i\left(\frac{\partial^2}{\partial Q_{i\xi}^2} + \frac{\partial^2}{\partial Q_{i\eta}^2} + \frac{\partial^2}{\partial Q_{i\zeta}^2}\right) \tag{2}$$

and

$$\mathcal{V}_0 = \frac{1}{2}\omega_1 Q_1^2 + \frac{1}{2}\omega_2(Q_{2\theta}^2 + Q_{2\epsilon}^2)$$
$$+ \frac{1}{2}\sum_{i=3}^{4}\omega_i(Q_{i\xi}^2 + Q_{i\eta}^2 + Q_{i\zeta}^2) \tag{3}$$

The change of electronic energy upon ionization is given by $\mathcal{W}$ in eq 1, which can be expressed as follows:[35−37]

$$\mathcal{W} = (E_0 + \kappa_1 Q_1)\mathbf{e}_\alpha + \lambda_2(Q_{2\theta}\mathbf{e}_\theta + Q_{2\epsilon}\mathbf{e}_\epsilon)$$
$$+ \sum_{i=3}^{4}\mu_i(Q_{i\xi}\mathbf{t}_\xi + Q_{i\eta}\mathbf{t}_\eta + Q_{i\zeta}\mathbf{t}_\zeta)$$
$$+ \frac{1}{2}[\gamma_1 Q_1^2 + \gamma_2(Q_{2\theta}^2 + Q_{2\epsilon}^2) + \sum_{i=3}^{4}\gamma_i(Q_{i\xi}^2 + Q_{i\eta}^2 + Q_{i\zeta}^2)]\mathbf{e}_\alpha$$
$$+ \frac{1}{2}\lambda_{22}[(Q_{2\epsilon}^2 - Q_{2\theta}^2)\mathbf{e}_\theta + Q_{2\theta}Q_{2\epsilon}\mathbf{e}_\epsilon]$$
$$+ \sum_{i=3}^{4}\mu_{ii}^{t_2}(Q_{i\eta}Q_{i\zeta}\mathbf{t}_\xi + Q_{i\xi}Q_{i\zeta}\mathbf{t}_\eta + Q_{i\xi}Q_{i\eta}\mathbf{t}_\zeta)$$
$$+ \frac{1}{4}\sum_{i=3}^{4}\mu_{ii}^{e}[(2Q_{i\zeta}^2 - Q_{i\xi}^2 - Q_{i\eta}^2)\mathbf{e}_\theta + \sqrt{3}(Q_{i\xi}^2 - Q_{i\eta}^2)\mathbf{e}_\epsilon]$$
$$+ \sum_{i=3}^{4}b_{2i}\left[\left(-\frac{1}{2}Q_{2\theta} + \frac{\sqrt{3}}{2}Q_{2\epsilon}\right)Q_{i\xi}\mathbf{t}_\xi\right.$$
$$\left. + \left(-\frac{1}{2}Q_{2\theta} - \frac{\sqrt{3}}{2}Q_{2\epsilon}\right)Q_{i\eta}\mathbf{t}_\eta + Q_{2\theta}Q_{i\zeta}\mathbf{t}_\zeta\right]$$
$$= \begin{pmatrix} \mathcal{W}_{11} & \mathcal{W}_{12} & \mathcal{W}_{13} \\ \mathcal{W}_{21} & \mathcal{W}_{22} & \mathcal{W}_{23} \\ \mathcal{W}_{31} & \mathcal{W}_{32} & \mathcal{W}_{33} \end{pmatrix} \tag{4}$$

where $\mathbf{e}_\alpha$, $\mathbf{e}_\theta$, and $\mathbf{e}_\epsilon$, as well as $\mathbf{t}_\xi$, $\mathbf{t}_\eta$, and $\mathbf{t}_\zeta$, are unitary (Pauli) matrices containing appropriate coupling coefficients: they are defined in the space of the $|\xi\rangle$, $|\eta\rangle$, $|\zeta\rangle$ vectors for the triply degenerate state at the reference geometry, along the totally symmetric (a_1) and components of the doubly degenerate (e) and triply degenerate (t_2) vibrational modes. The six matrices, as shown above, are given from left to right and top-down by[35,38]

$$\begin{pmatrix} 1 & 0 & 0 \\ 0 & 1 & 0 \\ 0 & 0 & 1 \end{pmatrix}, \begin{pmatrix} -\frac{1}{2} & 0 & 0 \\ 0 & -\frac{1}{2} & 0 \\ 0 & 0 & 1 \end{pmatrix}, \begin{pmatrix} \frac{\sqrt{3}}{2} & 0 & 0 \\ 0 & -\frac{\sqrt{3}}{2} & 0 \\ 0 & 0 & 0 \end{pmatrix}, \begin{pmatrix} 0 & 0 & 0 \\ 0 & 0 & 1 \\ 0 & 1 & 0 \end{pmatrix},$$
$$\begin{pmatrix} 0 & 0 & 1 \\ 0 & 0 & 0 \\ 1 & 0 & 0 \end{pmatrix}, \text{ and } \begin{pmatrix} 0 & 1 & 0 \\ 1 & 0 & 0 \\ 0 & 0 & 0 \end{pmatrix}$$

Thus, the various elements of the matrix Hamiltonian in eq 4 are as follows:

$$\mathcal{W}_{11} = E_0 + \kappa_1 Q_1 + \lambda_2\left(-\frac{1}{2}Q_{2\theta} + \frac{\sqrt{3}}{2}Q_{2\epsilon}\right)$$
$$+ \frac{1}{2}\left[\gamma_1 Q_1^2 + \gamma_2(Q_{2\theta}^2 + Q_{2\epsilon}^2) + \sum_{i=3}^{4}\gamma_i(Q_{i\xi}^2 + Q_{i\eta}^2 + Q_{i\zeta}^2)\right]$$
$$+ \frac{1}{2}\lambda_{22}\left(\frac{1}{2}Q_{2\theta}^2 - \frac{1}{2}Q_{2\epsilon}^2 + \sqrt{3}Q_{2\theta}Q_{2\epsilon}\right)$$
$$+ \frac{1}{4}\sum_{i=3}^{4}\mu_{ii}^{e}(2Q_{i\xi}^2 - Q_{i\eta}^2 - Q_{i\zeta}^2) \tag{5a}$$

$$\mathcal{W}_{22} = E_0 + \kappa_1 Q_1 + \lambda_2\left(-\frac{1}{2}Q_{2\theta} - \frac{\sqrt{3}}{2}Q_{2\epsilon}\right)$$
$$+ \frac{1}{2}\left[\gamma_1 Q_1^2 + \gamma_2(Q_{2\theta}^2 + Q_{2\epsilon}^2) + \sum_{i=3}^{4}\gamma_i(Q_{i\xi}^2 + Q_{i\eta}^2 + Q_{i\zeta}^2)\right]$$
$$+ \frac{1}{2}\lambda_{22}\left(\frac{1}{2}Q_{2\theta}^2 - \frac{1}{2}Q_{2\epsilon}^2 - \sqrt{3}Q_{2\theta}Q_{2\epsilon}\right)$$
$$+ \frac{1}{4}\sum_{i=3}^{4}\mu_{ii}^{e}(2Q_{i\eta}^2 - Q_{i\xi}^2 - Q_{i\zeta}^2) \tag{5b}$$

$$\mathcal{W}_{33} = E_0 + \kappa_1 Q_1 + \lambda_2 Q_{2\theta} + \frac{1}{2}\left[\gamma_1 Q_1^2 + \gamma_2(Q_{2\theta}^2 + Q_{2\epsilon}^2)\right.$$
$$\left. + \sum_{i=3}^{4}\gamma_i(Q_{i\xi}^2 + Q_{i\eta}^2 + Q_{i\zeta}^2)\right] + \frac{1}{2}\lambda_{22}(-Q_{2\theta}^2 + Q_{2\epsilon}^2)$$
$$+ \frac{1}{4}\sum_{i=3}^{4}\mu_{ii}^{e}(2Q_{i\zeta}^2 - Q_{i\xi}^2 - Q_{i\eta}^2) \tag{5c}$$

$$\mathcal{W}_{12} = \mathcal{W}_{21} = \sum_{i=3}^{4}(\mu_i Q_{i\zeta} + \mu_{ii}^{t_2}Q_{i\xi}Q_{i\eta} + b_{2i}Q_{2\theta}Q_{i\zeta}) \tag{5d}$$

$$\mathcal{W}_{13} = \mathcal{W}_{31}$$
$$= \sum_{i=3}^{4}\left[\mu_i Q_{i\eta} + \mu_{ii}^{t_2}Q_{i\xi}Q_{i\zeta} + b_{2i}\left(-\frac{1}{2}Q_{2\theta} - \frac{\sqrt{3}}{2}Q_{2\epsilon}\right)Q_{i\eta}\right] \tag{5e}$$

$$\mathcal{W}_{23} = \mathcal{W}_{32}$$
$$= \sum_{i=3}^{4}\left[\mu_i Q_{i\xi} + \mu_{ii}^{t_2}Q_{i\eta}Q_{i\zeta} + b_{2i}\left(-\frac{1}{2}Q_{2\theta} + \frac{\sqrt{3}}{2}Q_{2\epsilon}\right)Q_{i\xi}\right] \tag{5f}$$

The diagonal elements represent the diabatic potentials of the three components of this electronic state, while the off-diagonal elements are coupling terms. The vertical ionization energy of the $\tilde{X}^2T_2$ electronic state of CD_4^+ is denoted by E_0. In turn, the

linear coupling parameter of the totally symmetric a_1 vibrational mode is given by κ_1, and the linear JT coupling parameters for the doubly degenerate e and triply degenerate t_2 vibrational modes are denoted by λ_2 and μ_i, respectively. Note that γ_1, γ_2, and γ_i are the diagonal second-order parameters for the a_1, e, and t_2 vibrations, respectively. The diagonal second-order parameters (γ_i) actually take care of the frequency change, because of an electronic transition from the ground $\tilde{X}^1A_1$ electronic state of CD$_4$ to the cationic $\tilde{X}^2T_2$ state, respectively. In addition, b_{2i} represents the bilinear JT coupling parameters, which arise due to coupling between the e and t_2 modes. In turn, λ_{22}, μ_{ii}^e and $\mu_{ii}^{t_2}$ refer to the quadratic JT coupling constants resulting from the nontotally symmetric tensor convolutions of the $e \times e$ and $t_2 \times t_2$ symmetrized direct products, respectively. Numerical values of all the above coupling parameters are determined by performing extensive *ab initio* electronic structure calculations (see below).

2.2. Determination of Coupling Parameters. An accurate estimation of the coupling parameters of the above-mentioned Hamiltonian matrix is done by calculating the adiabatic electronic PESs of the $\tilde{X}^2T_2$ electronic state of CD$_4^+$ along the dimensionless normal coordinates of ground-state ($\tilde{X}^1A_1$) methane. Geometry optimization and calculation of harmonic vibrational frequencies of equilibrium CD$_4$ in its ground state ($^1A_1$) have been carried out at the second-order Møller−Plesset perturbation (MP2) level of theory, using the correlation-consistent polarized valence triple-ζ (cc-pVTZ) basis set of Dunning[39] with the Gaussian 03 program.[40] The definition of the dimensionless normal coordinates are retained as in our previous studies[19,20,26] and given in Table 1, along with it is experimental counterpart.[41]

Table 1. Description of the Vibrational Modes of the Electronic Ground State of CD$_4$ Computed at the MP2/cc-pVTZ Level of Theory (All Values Are Given in eV)[a]

mode	Frequency, ω_i		Predominant nature	coordinate
	this work	exp[b]		
$\nu_1(a_1)$	0.26984	0.26148	symmetric stretching	Q_1
$\nu_2(e)$	0.13911	0.13539	bending deformation	$Q_{2\theta}, Q_{2\epsilon}$
$\nu_3(t_2')$	0.29491	0.28008	asymmetric stretching	$Q_{3\xi}, Q_{3\eta}, Q_{3\zeta}$
$\nu_4(t_2)$	0.12649	0.12349	bending deformation	$Q_{4\xi}, Q_{4\eta}, Q_{4\zeta}$

[a]While the theoretical frequencies are harmonic in nature, the experimental ones are fundamentals. [b]Data taken from ref 41.

The diabatic coupled surfaces of the $\tilde{X}^2T_2$ electronic manifold of CD$_4^+$ are constructed by calculating the associated adiabatic *ab initio* energies along one and two dimensions in the normal mode coordinate space of CD$_4$. Complete-active-space self-consistent-field (CASSCF) calculations have been performed to optimize the molecular orbitals, followed by multireference configuration-interaction (MRCI) calculations to account for the dynamic correlation using the full-valence-complete-active-space (FVCAS) wave function as reference. In this, the C 1s core orbitals have been kept closed, but optimized in the CASSCF step. However, in the MRCI calculations, such core orbitals were kept frozen. Therefore, the FVCAS reference wave function involves seven correlated electrons in eight active orbitals, amounting to a total of 2352 configuration state functions. The cc-pVTZ basis set of Dunning[39] has been utilized for the calculations, which were performed with the Molpro package.[42] The eigenvalues of the above 3 × 3 diabatic

Hamiltonian matrix (excluding the kinetic energy of the nuclei) have then been fitted to the adiabatic *ab initio* ionization energies by a least-squares procedure to derive numerically the various coupling parameters and, hence, the adiabatic PESs.[43,44]

The procedure involved three steps. First, the vertical ionization energy of the three sheets of the $\tilde{X}^2T_2$ electronic manifold has been calculated by distorting the initial T_d geometry along the ith vibrational mode (keeping others at their equilibrium value) at intervals of 0.5 over the range of $0 \leq |Q_i| \leq 6$. The PESs obtained were then used to determine the various coupling parameters of the one-dimensional (1D) potential of the model Hamiltonian described in section 2.1. In the second step, the vertical ionization energies were calculated for the simultaneous displacements of two components of e mode coordinate, two components of the t_2 mode coordinates, and one component of the e and t_2 mode coordinates. Note that, in all three cases, both coordinates are varied by an equal amount. Finally, all coupling parameters of the vibronic Hamiltonian in eq 4 were fitted to *ab initio* energies obtained from the above distorted geometries along the diagonal of this 2D nuclear coordinate subspace, with the coupling parameters estimated from the 1D cuts as initial guess. The optimum fitted parameters so obtained are given in Table 2.

Table 2. Coupling Parameters in eqs 1−5f, As Obtained from CASSCF/MRCI Calculations (All Values Are Given in eV)[a]

mode	$\kappa_1/\lambda_2/\mu_i$	$\gamma_{1/2/i}$	$\lambda_{22}/\mu_{ii}^{t_2}$	μ_{ii}^e	b_{2i}
$\nu_1(a_1)$	0.2854	0.0131			
$\nu_2(e)$	0.5612	−0.0360	−0.0139		
$\nu_2(t_2')$	0.3206	0.0059	−0.0064	−0.0342	−0.0185
$\nu_4(t_2)$	0.3337	−0.0434	−0.0242	−0.0129	0.0330
IP	14.3447				

[a]The vertical ionization energy of the $\tilde{X}^2T_2$ electronic state of CD$_4^+$ is also given.

2.3. Dynamic Observables. The dynamic variables are obtained from the vibronic energy level spectrum of the $\tilde{X}^2T_2$ electronic manifold of CD$_4^+$ calculated with the above Hamiltonian. The intensity, $P(E)$, of the vibronic band is obtained using Fermi's golden rule:

$$P(E) = \sum_v |\langle \Psi_v^f | \hat{T} | \Psi_0^i \rangle|^2 \delta(E - E_v^f + E_0^i) \quad (6)$$

where $|\Psi_v^f\rangle$ represents the eigenstates of the vibronic Hamiltonian with energy E_v^f, and $|\Psi_0^i\rangle$ is the initial ground vibronic state of the neutral molecule with energy E_0^i. $\hat{T}$ is the operator that describes the interaction of the electrons with the external radiation, and E the electron binding energy (ionization energy). In turn, the initial vibronic state

$$|\Psi_0^i\rangle = |\Phi_0\rangle|\chi_0^0\rangle \quad (7)$$

is represented as a product of the diabatic electronic ($|\Phi_0\rangle$) and vibrational ($|\chi_0^0\rangle$) components. The latter is the eigenfunction of the unperturbed reference Hamiltonian, $\mathcal{H}_0$. Note that the scattering wave function of the outgoing electron is missing in the final vibronic state, $|\Psi_v^f\rangle$. Similarly, the kinetic energy of the outgoing electron is missing in the Einstein condition of eq 6.

3609

dx.doi.org/10.1021/ct500388k | J. Chem. Theory Comput. 2014, 10, 3606−3616

In fact, the determination of the correct wave function of the final vibronic state is actually an intricate problem, because of the fact that the scattering state is a plane wave at asymptotic distances; however, for shorter ones, this is modified, because of interaction with the cation, which is a topic that is actually an active research area in electron-scattering theory. Such a theoretical formulation is even harder for HHG spectroscopy, since the cation and continuum electron are in this case created under an intense laser field. It should also be noted that the calculation of vibronic intensities close to the ionization threshold poses an additional intricacy by the fact that it should verify the Wigner threshold law.[45] In the present case, we have used Franck−Condon factors to calculate the vibronic intensities for the $\tilde{X}^2T_2$ state of CD_4^+.

In a time-dependent picture, eq 6 can be related to a Fourier transform of the time autocorrelation function of the WP:[46]

$$P(E) \approx 2Re \int_0^\infty e^{iEt/\hbar} \langle 0|\tau^\dagger e^{-i\mathcal{H}t/\hbar} \tau|0\rangle \, \mathrm{d}t \quad (8)$$

$$\approx 2Re \int_0^\infty e^{iEt/\hbar} C^m(t) \, \mathrm{d}t \quad (9)$$

The term $C^m(t)$ is the time autocorrelation function of the WP initially prepared on the mth electronic state ($C^m(t) = \langle \Psi^m(0)|\Psi^m(t)\rangle$), and τ is the transition dipole matrix ($\tau^\dagger = (\tau^{\overline{X_1}}, \tau^{\overline{X_2}}, \tau^{\overline{X_3}})$, with $\tau^m = \langle \Phi_m|\hat{T}|\Phi_0\rangle$; the dagger denotes "transposed", and $\tilde{X}_i$ ($i = 1 - 3$) for the various degenerate potential sheets. As discussed above, we assume that the ejected electron does not correlate with the electrons of the ion: therefore, the involved matrix elements are set to unity. This is consistent with the applicability of the Franck−Condon approximation in a diabatic electronic basis.[45] The partial spectra are calculated by propagating WPs for three different initial conditions, which are then convoluted together to yield the final composite vibronic spectrum.

In a time-dependent method, an appropriate WP is first prepared in the final electronic state of the cation and then propagated with the aid of the time-dependent Schrödinger equation, $i\hbar\partial_t|\Psi_v\rangle = \mathcal{H}|\Psi_v\rangle$. The autocorrelation function, $C^m(t)$, of the WP is recorded in time and Fourier-transformed to finally calculate the vibronic spectrum via eqs 8 and 9. The WP propagation is carried out by employing the efficient MCTDH algorithm,[21−25] which is best-suited for full quantum mechanical simulation of multistate and multimode problems, such as the present one. The multiset ansatz of the MCTDH algorithm allows a combination of vibrational degrees of freedom to effectively reduce the dimensionality problem. The WP associated with each electronic state is described using a different set of single particle functions (SPFs). By combining the nuclear degrees of freedom f, p particles are formed ($p < f$), with the variables for the p sets of SPFs being defined in terms of the single- or multidimensional coordinates of a particle. The operational MCTDH algorithm is discussed in detail in the literature,[24,25] and we do not reiterate it here.

3. RESULTS AND DISCUSSION

3.1. Adiabatic Potential Energy Surfaces. An examination of the topography of the adiabatic PESs for the $\tilde{X}^2T_2$ electronic state of CD_4^+ near the JT conical intersection is performed here, using the above vibronic Hamiltonian (eqs 1−5f). The resulting 1D cuts of the multidimensional PESs along a single dimensionless normal coordinate, keeping all

others at equilibrium, $\mathbf{Q} = \mathbf{0}$, are shown in Figures 1 and 2. Specifically, Figure 1 shows 1D cuts of the potential energy

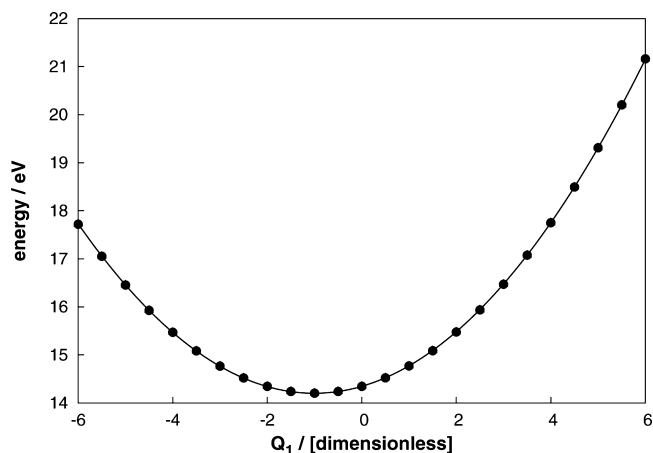**Figure 1.** Adiabatic potentials for the $\tilde{X}^2T_2$ state of CD_4^+ along the dimensionless totally symmetric vibrational mode ν_1. Energy of the ground electronic state of CD_4 ($\tilde{X}^1A_1$) at equilibrium configuration ($\mathbf{Q} = \mathbf{0}$) is set to zero. The present vibronic model is shown by the solid line and the computed *ab initio* data is represented by the solid dots.

hypersurface of ground-state CD_4^+ plotted along the totally symmetric (a_1) stretching mode (ν_1). As shown, the degeneracy of the $\tilde{X}^2T_2$ electronic manifold is unaffected upon distortion along the symmetric vibrational mode. However, it alters the nuclear dynamics by tuning the position of the minimum of the seam of the JT conical intersection: the minimum is predicted to be $\mathcal{V}_{\min}^{(c)} \approx 14.2008$ eV, whereas, for CH_4^+, it was ~14.1813 eV. Similarly, the 1D *ab initio* potential energy cuts along both components ($Q_{2\theta}$ and $Q_{2\epsilon}$) of the doubly degenerate (e) scissoring mode (ν_2) are presented in Figures 2a and 2b. The two sets of potential energy cuts shown in Figures 2a and 2b reveal that the nuclear displacements along the $Q_{2\epsilon}$ component splits the triple degeneracy of the $\tilde{X}^2T_2$ electronic manifold into three components, while the one along the $Q_{2\theta}$ component yields a partial lifting, namely, one single component plus one double degenerate component. Thus, we fitted them simultaneously with the best results depicted in
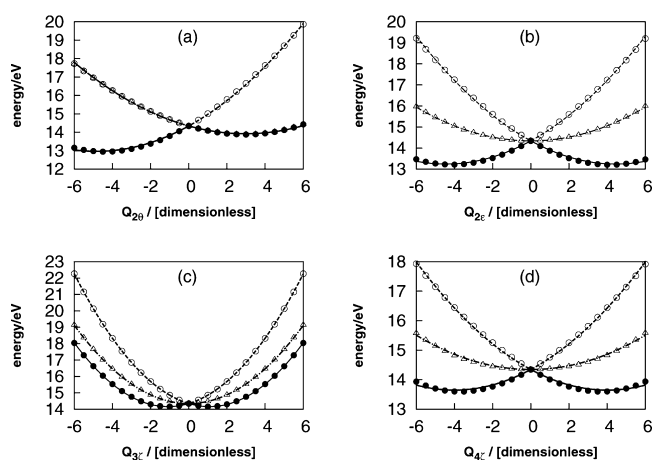

Figure 2. Adiabatic potentials for the $\tilde{X}^2T_2$ state of CD_4^+ along both components (θ and ϵ) of the e and the ζ component of the t_2 vibrational modes, respectively.

Figures 2b and 2a, respectively. The electronic degeneracy of the $\tilde{X}^2T_2$ state is also lifted when distorting along the triply degenerate modes ν_3 and ν_4, with the split yielding a total of three states. Note that any of the three vibrational components (Q_ξ, Q_η, and Q_ζ) lift the triple electronic degeneracy in a similar way for a given t_2 mode; hence, for the sake of brevity, we have shown cuts only along one component. The resulting potential energy cuts along the Q_ζ component of the vibrational modes ν_3 and ν_4 are illustrated in Figures 2c and 2d, respectively. It can be seen that the current model mimics well all *ab initio* data points. Within a first-order coupling approach, the JT stabilization energy due to the formation of new minima on the lowest adiabatic sheet of the JT split $\tilde{X}^2T_2$ state along the doubly degenerate ν_2 vibrational mode is predicted to be $\lambda_2^2/(2\omega_2) \approx 1.1320$ eV, while the one due to triply degenerate ν_3 and ν_4 is $\sum_{i=3}^{4}(2\mu_i^2/(3\omega_i)) \approx 0.8193$ eV. For CH_4^+, the corresponding values are ~1.113 and ~0.802 eV.

In the following, we examine the adiabatic potential energy cuts along the diagonal of the 2D subspace of the nuclear coordinates obtained by simultaneously displacing two JT active e and t_2 modes. For this purpose, we consider the following three possible combinations of coordinates that manifest nonvanishing JT couplings on a 2D subspace: (i) the two coordinates correspond to the two components of the e mode; (ii) both belong to one t_2 mode (the possibility of combining the other t_2 mode has been ignored for simplicity); (iii) one belongs to the e mode and the other to the t_2 mode. The full matrix is fitted to the calculated *ab initio* data points, and the results are shown in Figures 3 and 4.
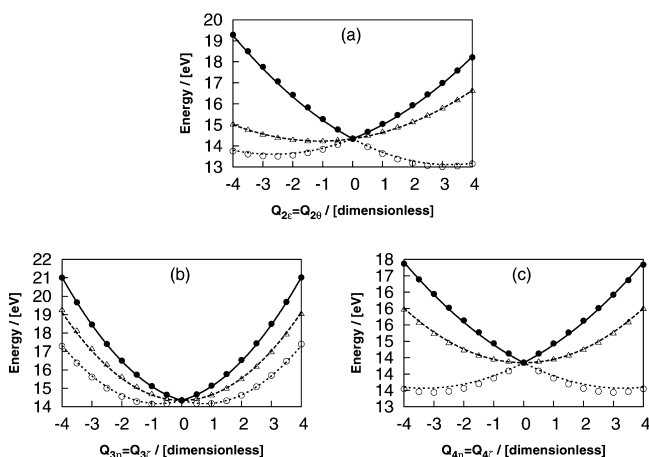

Figure 3. Adiabatic potentials for the $\tilde{X}^2T_2$ state of CD_4^+ along the simultaneous displacement of two coordinates of e and t_2 vibrational modes, respectively.

Clearly, the potential energy cuts shown above indicates that the current diabatic model Hamiltonian reproduces the *ab initio* data well. A comparison of various critical points estimated on those hypersurfaces with the same predicted on $\tilde{X}^2T_2$ electronic manifold of CH_4^+ illustrates that the static aspects of these two isotopomers are almost identical, as they should be. Of course, the difference arises in nuclear motion due to different nuclear masses and should have impact on the dynamical observables, i.e., on the vibronic spectra.

3.2. Photoelectron Spectra. In this subsection, we present the photoelectron spectra obtained by employing the above vibronic Hamiltonian (cf., eqs 1−5f). Since it is the same for CH_4 already reported elsewhere,[19,26] here, we examine only the
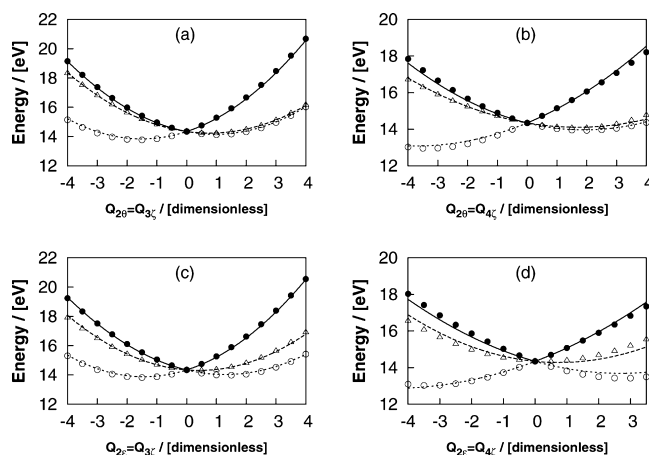

Figure 4. Adiabatic potentials for the $\tilde{X}^2T_2$ state of CD_4^+ along the simultaneous displacement of two coordinates of one component of e mode and one component of t_2 vibrational modes.

spectra of CD_4. However, for the sake of completeness, we compare both in Figure 5, along with the experimental He I
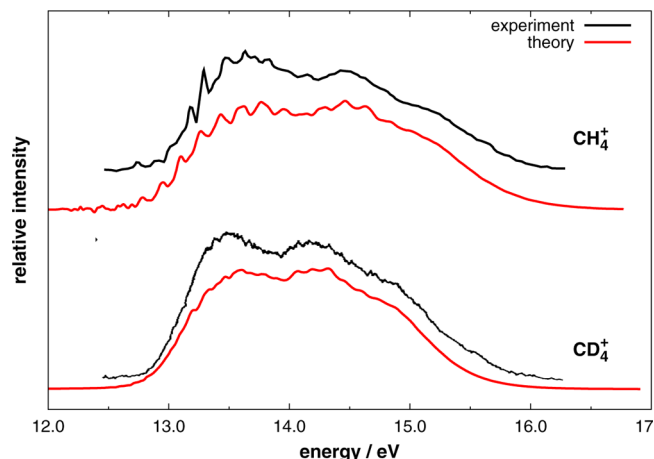

Figure 5. Vibronic band of the $\tilde{X}^2T_2$ electronic state of CH_4^+ and CD_4^+. The intensity (in arbitrary units) is plotted along the energy (relative to minimum of the $\tilde{X}^1A_1$ state of CH_4 and CD_4) of the final vibronic states.

photoelectron spectra.[47] As discussed in the previous subsection, all nine vibrational modes may have an important role on the structure of this photoelectron band. Therefore, we follow the nuclear dynamics simultaneously on the three diabatically coupled sheets of the $\tilde{X}^2T_2$ electronic manifold, including all nine vibrational degrees of freedom. This leads to a Hamiltonian matrix of huge dimension, and the associated Schrödinger equation cannot be solved by direct diagonalization. Thus, we solve the Schrödinger equation by propagating WPs within a time-dependent framework using the MCTDH algorithm,[21−25] and we obtain the eigenvalue spectrum. The normal mode combinations, sizes of primitive and single particle bases to prepare the WP for CD_4^+ (identical to CH_4^+) are shown in Table 3.

Three calculations are carried out by initially preparing the WP separately on each component of the $\tilde{X}^2T_2$ electronic manifold. The WP is propagated for 200 fs in each calculation. The time autocorrelation functions from the above three calculations are combined, damped with an exponential

Table 3. Normal Mode Combinations, Sizes of Both Primitive and Single-Particle Basis Used for Propagating WP on the Diabatically Coupled Electronic Manifold Employing the Complete Vibronic Hamiltonian of eqs 1−5f

normal modes[a]	primitive basis[b]	SPF basis[c]	Figure
$(\nu_1, \nu_{3\eta}, \nu_{4\zeta})$	(12, 15, 10)	[10, 9, 8]	
$(\nu_{2\epsilon}, \nu_{3\xi}, \nu_{4\eta})$	(25, 15, 10)	[10, 9, 8]	5
$(\nu_{3\zeta}, \nu_{4\xi}, \nu_{2\theta})$	(15, 10, 25)	[9, 8, 7]	

[a]Vibrational degrees of freedom (DOF), which are combined to particles. [b]Number of primitive basis functions for each DOF. [c]Number of single particle functions (SPFs) for each JT split electronic state.

function to account for experimental line broadening effects (e^{-t/τ_r} (with $\tau_r = 22$ fs)), and finally Fourier-transformed to calculate the vibronic band of this $\tilde{X}^2T_2$ electronic state. The value of τ_r used in the damping function corresponds to a convolution of the vibronic line spectrum with a Lorentzian function of 60 meV (full width at half maximum, fwhm). The simulated spectrum envelope displayed in Figure 5, is in good agreement with the experimental spectrum.[47] Both the characteristic line structure and the spectral intensity and width of the vibronic band are well-reproduced by the present QVC scheme.

In the following, we compare the dominant vibrational progressions predicted from the current model Hamiltonian with the experimental ones. For such a comparison, we first construct various reduced-dimensionality models in terms of a_1, e, and t_2 vibrational modes, and examine the vibrational energy levels separately. These results help to understand the role of various vibrational modes in the complex vibronic structure of CD_4^+ ($\tilde{X}^2T_2$). The vibronic energy eigenvalues are obtained by diagonalizing the Hamiltonian matrix using the Lanczos algorithm.[48] The fundamental and overtones up to third-order are excited for the ν_1 mode. A corresponding peak spacing of ∼0.2763 eV can be estimated from the calculated partial spectrum for the ν_1 vibration. A similar spectrum due to the ν_2 vibrational mode reveals an extended progression due to its large JT coupling (cf., Table 2). A line spacing of ∼0.1275 eV is predicted. The partial spectrum due to both t_2 vibrations has also been calculated. The intense lines are spaced relative to the band origin, ∼0.3338 eV and ∼0.0793 eV, corresponding to the frequency of the ν_3 and ν_4 vibrational modes, respectively. However, the JT activity of the triply degenerate asymmetric scissoring mode ν_4 is stronger than the triply degenerate asymmetric stretching mode ν_3. Thus, ν_4 scissoring mode forms the dominant progression underlying the partial spectrum obtained due to t_2 modes.

A comparison of the two vibronic bands of $\tilde{X}^2T_2$ electronic manifold of CH_4^+ and CD_4^+ in Figure 5 shows that the photoelectron band is wider for CH_4. However, the JT stabilization energies estimated from our calculations are similar for both isotopomers. Therefore, the smaller width of the photoelectron spectra of CD_4 may be attributed to the lower vibrational frequencies of this heavier isotope: a mass effect on nuclear dynamics.

4. BEYOND FEMTOSECOND DYNAMICS

Although the role of the ejected photoelectron has been explicitly neglected above, it can actually play a key role in examining the vibrational structure of the cation in a subfemtosecond window. In fact, the electron WP that is generated by the femtosecond laser pulse will recollide with the cation after a time delay, which leads to the harmonic emission, with successively higher harmonics generated at longer time delays.[49] It is this property of the high-harmonic radiation that allows us to probe the nuclear motion over a range of pump–probe time delays set by the temporal spread of the recolliding electron WP. Suffice it to recall at this point that the time up to which the mapping of harmonic order is possible is typically only ∼1.6 fs in a 800-nm laser field. In this section, we investigate the subfemtosecond nuclear dynamics on a three-fold degenerate electronic state by establishing the involved adiabatic PESs including nonadiabatic coupling effects. We then follow previous work[13,18] where even ignoring the explicit treatment of the outgoing electron WP led to extract crucial information on the motion of the nuclei in subfemtosecond regime. The analysis stems from the semiclassical three-step model of HHG as described in the Introduction. The intensity of the high-harmonics, so generated, is approximately proportional to the squared modulus of the nuclear autocorrelation function, $C_{nu}(t) = \langle \chi(0)|\chi(t)\rangle$, where $\chi(0)$ and $\chi(t)$ are, respectively, the initial and propagated nuclear WP of the cationic wave function evolved from the moment of ionization until the moment of recollision.[4,10] Recall now that within the Condon approximation, the transition dipole matrix from neutral ground electronic state (Φ_0) to the cationic electronic state (Φ_m), $\tau^m = \langle \Phi_m|\hat{T}|\Phi_0\rangle$, is assumed to be independent of nuclear coordinates. Thus, the ratio of the high-harmonic spectra of CD_4 relative to CH_4 can be approximately mapped onto the autocorrelation function ratio (see eq 10):[4,10]

$$\text{autocorrelation function ratio} = \frac{|C_{CD_4}(t)|^2}{|C_{CH_4}(t)|^2} \tag{10}$$

However, in strong-field ionization, the transition dipole matrix depends on the nuclear geometry.[14] The reason for this is the exponential dependence of the strong-field ionization rate on the electronic binding energy. Accordingly, the Franck–Condon approximation is expected to break down.[14,15,50] Following previous work,[13] we note that eq 10 assumes both the ionization and recombination amplitudes to be independent of the nuclear geometry, and the PESs of both neutral and ionic species not affected by the laser field. Despite the fact that eq 10 is approximate, it is very useful for studying polyatomic molecules, where the exact treatment is prohibitively expensive.

The autocorrelation functions have been calculated using the above devised QVC Hamiltonian in the full 9D space of the nuclear vibrations. The results shown in Figure 6 are for the lowest adiabatic sheet of the $\tilde{X}^2T_2$ electronic manifold. The autocorrelation functions estimated for the remaining two sheets are numerically similar and hence are not shown for brevity. A magnified view of the autocorrelation functions up to 50 fs is shown in the inset of Figure 6 for enhanced visibility. The ratio of the squared modulus of the autocorrelation functions between CD_4^+ and CH_4^+ is shown by the solid blue line in Figure 7. Despite the assumption involved in our approach, the results show good agreement with the recent experimental recordings of Baker et al.[4] Note that our result predicts the intensity of the harmonic signal to be larger for the heavier isotope as it should be due to the much slower motion of the nuclei, an effect that is found to be enhanced for longer time-evolution.

From the structural point of view, earlier investigations have revealed that the JT distortion leads to the minimum energy
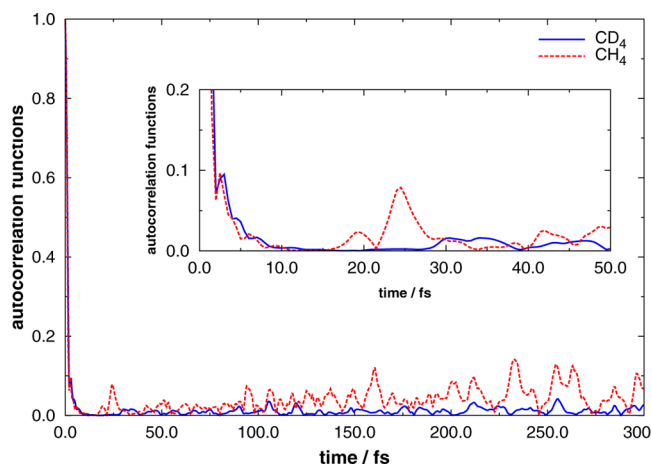
Figure 6. Autocorrelation functions for the lowest adiabatic sheet of the $\tilde{X}^2 T_2$ electronic state of CH_4^+ and CD_4^+. Red dashed lines correspond to CH_4^+, and blue solid lines correspond to CD_4^+. For better resolution, the inset shows the same only up to 50 fs. All quantities are calculated from the present QVC model.
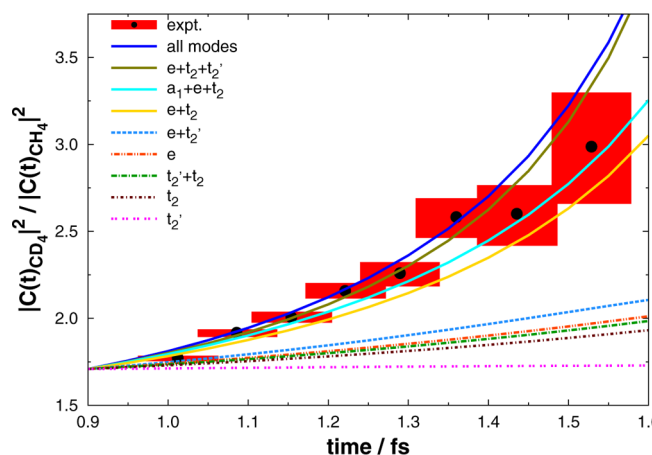

Figure 7. Ratio of the squared autocorrelation functions of CD_4^+ and CH_4^+ in various dimensional spaces of nuclear vibrations along with experimental recordings of the ratio of the harmonic intensity.[4] Legend: solid lines, this work; solid boxes, experimental. For a better comparison with experimental recordings and reduced dimensional results, the calculated ratios have been vertically shifted approximately by t_2', 0.690; t_2, 0.625; $t_2' + t_2$, 0.603; e, 0.587; $e + t_2'$, 0.558; $e + t_2$, 0.466; $a_1 + e + t_2$, 0.425; $e + t_2 + t_2'$, 0.426; $a_1 + e + t_2 + t_2'$, 0.387.

structure of the CH_4^+, namely to a distorted geometry of C_{2v} symmetry (compare to the T_d geometry of CH_4).[51] Experimental evidence for that C_{2v} geometry was also observed by Knight et al.[52] via electron spin resonance spectroscopy experiments in a neon matrix and by Vager et al.[53] from Coulomb explosion experiments. Subsequently, the above structural transformation at the moment of ionization can be anticipated to be an extremely fast process since the bond angle ($\angle H-C-H = 109.5°$) of the T_d structure of CH_4 is far from the equilibrium bond angle ($\angle H-C-H < 60°$) in CH_4^+. Indeed, we estimate the time scale for this structural rearrangement to be of the order of a few femtoseconds, as illustrated by the solid blue line in Figure 7. We have then corroborated the subfemtosecond time scale of the above rearrangement by starting from the nonadiabatically coupled PESs of $\tilde{X}^2 T_2$ electronic manifold, and using the JT theorem.

The ratio of nuclear autocorrelation functions is expected to be dependent on the nuclear vibrations due to the imperfect overlap of the initial and propagated vibrational WPs, with respect to the number of nuclear degrees of freedom involved in the calculations. Therefore, we have modeled various reduced dimensionality Hamiltonians to examine the effect of nuclear vibrations on the autocorrelation functions. The resultant ratios of autocorrelation functions are displayed in Figure 7. Note that, for a better comparison with the various reduced dimensional results, we have vertically shifted all calculated ratios of the squared autocorrelation functions such as to set them at ~1.7 for a time delay of 0.9 fs. It should also be noted that the shifting is larger for the lower dimensional results due to the smaller overlap between initial and propagated WPs (see the figure caption for Figure 7). As it can be seen from Figure 7, a 5D dynamics study consisting of a doubly degenerate (e) and a triply degenerate (t_2) bending mode is a minimum required to mimic the experimental recordings. Any larger dimensional calculations show about equally good agreement with experiment. However, lower-dimensional calculations (compare to the above 5D model) severely fail to reproduce the experimental observations. Therefore, our results provide the first direct evidence that the structural rearrangement from T_d to C_{2v} geometry in CH_4^+ occurs via the 5D combination of modes of e and t_2 symmetry. An epikernel principle predicts two possible mechanism for such symmetry reduction due to JT distortion: (a) along the 5D combination mode of e and t_2 symmetry, and (b) via triply degenerate t_2 vibrational mode.[37] Our results ruled out the later possibility and established the mechanism for structural rearrangement in CH_4^+ to be along 5D hypersurfaces formed by bending vibrations of e and t_2 symmetry. A schematic representation is shown in Figure 8.
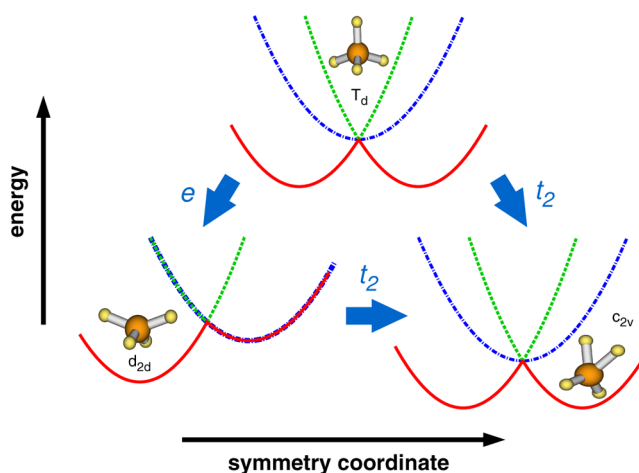

Figure 8. Schematic representation of the structural rearrangement of CH_4^+ from geometries with T_d to C_{2v} symmetries due to JT distortion.

We already estimated that the intensity of the harmonic signal is greater for the heavier isotope of methane, and such a phenomenon is enhanced with longer time evolution up to ~1.6 fs, which agrees well with the experimental observation.[4] This experiment was done by using a wavelength of 800 nm and, hence, the time at which the nuclear dynamics can be monitored is limited to ~1.6 fs.[4] Recently, Kraus and Wörner extended the time window to ~3.6 fs by investigating ND_3/NH_3 with wavelengths up to 1800 nm. In fact, even longer

3613

dx.doi.org/10.1021/ct500388k | J. Chem. Theory Comput. 2014, 10, 3606−3616

wavelengths (up to 3.5 μm) have been used for Rb atoms.[54] However, to our knowledge, no such experiment is available for CD_4/CH_4 with wavelengths beyond 800 nm. This need for an accurate theoretical description of longer time intervals has actually been part of our motivation to further calculate the ratio of the square of the autocorrelation functions of CD_4^+ and CH_4^+ over longer time-windows. It will enable extracting nuclear dynamics information over much wider temporal resolutions for which experimental data are as yet unavailable. As above, all calculations have been done by employing the full-dimensional diabatic Hamiltonian, with the results being shown in Figure 9.
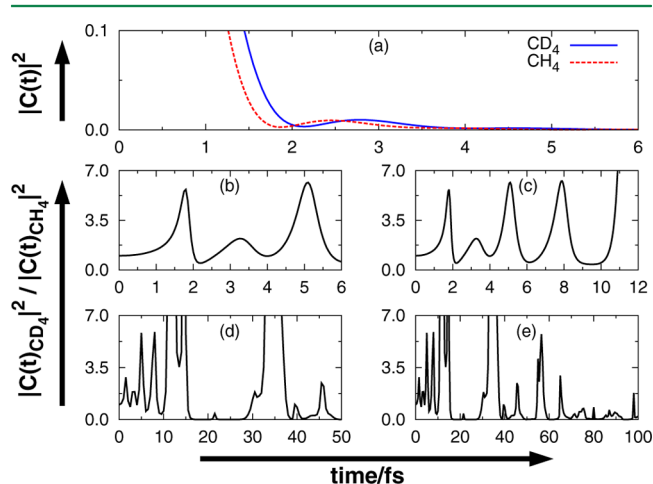

Figure 9. (a) Squared autocorrelation functions for the lowest adiabatic sheet of the $\tilde{X}^2T_2$ electronic state of CD_4^+ and CH_4^+. Also shown is the ratio of squared autocorrelation functions of CD_4^+ and CH_4^+ up to (b) ~6 fs of time evolution, (c) ~12 fs of time evolution, (d) ~50 fs of time evolution, and (e) ~100 fs of time evolution.

Figure 9a displays the square of the modulus of the autocorrelation functions for the lowest adiabatic sheet of $\tilde{X}^2T_2$ electronic state of CD_4^+ and CH_4^+. Figures 9b and 9c show that the ratio of the autocorrelation functions develops a maximum at ~1.85 fs. (A similar maximum was also found for ND_3/NH_3.[17,18]) The reason for the occurrence of such a maximum may be attributed to the fact that the squared autocorrelation function of CH_4^+ had already reached its lowest value at ~1.85 fs, while for CD_4^+, it is still decreasing with time, as shown in Figure 9a. Thus, our results predict that the structural rearrangement of CH_4^+ from T_d to C_{2v} geometry is likely to take place within ~1.85 fs. Figures 9b and 9c further show recurrences of such maxima at ~3.30 fs and ~5.10 fs. Accordingly, the average time difference among those maxima could be anticipated as the oscillation time between T_d and C_{2v} configurations of CH_4^+. Obviously, very accurate evidence can be gained by examining the time evolution of the WP on the above 5D hypersurfaces, an issue beyond the scope of the present work. Finally, the autocorrelation function ratio up to 50 and 100 fs is shown in Figures 9d and 9e. As expected, the ratio shows irregular behavior for such a long time-delay due to the pronounced anharmonicity of the nuclear motions.

5. SUMMARY AND OUTLOOK

We have carried out a detailed quantum nuclear dynamics study on the triply degenerate ($\tilde{X}^2T_2$) ground electronic manifold of the methane cation and its deuteriated isomer in the subfemtosecond regime. While so doing, we have first performed a femtosecond dynamics study by probing the first photoelectron band of both CH_4 isotopomers, then followed by exploration of the subfemtosecond nuclear dynamics by simulating the ratio of the intensity of the harmonic signals recorded in high-harmonic generation spectroscopy. The necessary Hamiltonian has been constructed from extensive *ab initio* electronic structure calculations employing multi-reference configuration interaction method and the underlying PESs have been established through various one-dimensional (1D) and two-dimensional (2D) cuts on the normal-mode coordinate space of the neutral species. To get them into analytic form, various coupling parameters of the vibronic Hamiltonian have been estimated by fitting the eigenvalues of the matrix Hamiltonian to the computed *ab initio* adiabatic potentials along each of the nine vibrational modes and their 2D combinations thereof. First principles calculations have then been carried out with time-dependent quantal methods to simulate the nonadiabatic nuclear motion on this coupled electronic manifold. Like CH_4^+ in our previous study,[19,26] we also found here that the ν_2 vibration is strongly excited in CD_4^+, because of large Jahn−Teller (JT) coupling and the JT activity of the triply degenerate bending mode (ν_4) is stronger than the triply degenerate stretching mode (ν_3). We have further estimated the JT stabilization energies as ~1.132 and ~0.802 eV for the e and t_2 vibrations, which are again nearly identical with CH_4^+. However, the first photoelectron band of CD_4 has been shown to be narrow compared to CH_4, which we have rationalized as a mass effect on the nuclear dynamics observables.

In summary, we have calculated the ratio of squared autocorrelation functions of the title cation and its deuterated isotopomer and found that the intensity of the high-harmonic signal is greater for heavier isotopes and this trend is enhanced up to ~1.85 fs. From this observation, we predicted that the structural rearrangement of CH_4^+ from T_d to C_{2v} configuration occurs in ~1.85 fs. This has also allowed to propose the mechanism for the rearrangement via a 5D hypersurface developed from the JT distorted bending vibrations of e and t_2 symmetry. Finally, we have estimated the recurrences of the first maximum at time evolutions of ~3.25 and ~5.10 fs. This allowed to anticipate that the average time difference between such maxima could be the oscillation time between T_d and C_{2v} CH_4^+.

AUTHOR INFORMATION

Corresponding Author

*E-mail: varandas@uc.pt.

Notes

The authors declare no competing financial interest.

■ REFERENCES

(1) Niikura, H.; Lgar, F.; Hasbani, R.; Bandrauk, A. D.; Ivanov, M. Y.; Villeneuve, D. M.; Corkum, P. B. Sub-laser-cycle Electron Pulses for Probing Molecular Dynamics. *Nature* **2002**, *417*, 917−922.

(2) Niikura, H.; Légaré, F.; Hasbani, R.; Ivanov, M. Y.; Villeneuve, D. M.; Corkum, P. B. Probing Molecular Dynamics with Attosecond Resolution Using Correlated Wave Packet Pairs. *Nature* **2003**, *421*, 826−829.

(3) Kienberger, R.; Goulielmakis, E.; Uiberacker, M.; Baltuska, A.; Yakovlev, V.; Bammer, F.; Scrinzi, A.; Westerwalbesloh, T.; Kleineberg, U.; Heinzmann, U.; Drescher, M.; Krausz, F. Atomic Transient Recorder. *Nature* **2004**, *427*, 817−821.

(4) Baker, S.; Robinson, J. S.; Haworth, C. A.; Smith, R. A.; Chirila, C. C.; Lein, M.; Tisch, J. W. G.; Marangos, J. P. Probing Proton Dynamics in Molecules on an Attosecond Time Scale. *Science* **2006**, *312*, 424−427.

(5) Corkum, P. B. Plasma Perspective on Strong Field Multiphoton Ionization. *Phys. Rev. Lett.* **1993**, *71*, 1994−1997.

(6) Schafer, K. J.; Yang, B.; DiMauro, L. F.; Kulander, K. C. Above Threshold Ionization Beyond the High Harmonic Cutoff. *Phys. Rev. Lett.* **1993**, *71*, 1599−1602.

(7) Kulander, K. C.; Cooper, J.; Schafer, K. J. Laser-assisted Inelastic Rescattering During Above-threshold Ionization. *Phys. Rev. A* **1995**, *51*, 561−568.

(8) Sansone, G.; Benedetti, E.; Calegari, F.; Vozzi, C.; Avaldi, L.; Flammini, R.; Poletto, L.; Villoresi, P.; Altucci, C.; Velotta, R.; Stagira, S.; Silvestri, S. D.; Nisoli, M. Isolated Single-cycle Attosecond Pulses. *Science* **2006**, *314*, 443−446.

(9) Goulielmakis, E.; Schultze, M.; Hofstetter, M.; Yakovlev, V. S.; Gagnon, J.; Uiberacker, M.; Aquila, A. L.; Gullikson, E. M.; Attwood, D. T.; Kienberger, R.; Krausz, F.; Kleineberg, U. Single-Cycle Nonlinear Optics. *Science* **2008**, *320*, 1614−1617.

(10) Lein, M. Attosecond Probing of Vibrational Dynamics with High-Harmonic Generation. *Phys. Rev. Lett.* **2005**, *94*, 053004−053007.

(11) Kanai, T.; Takahashi, E. J.; Nabekawa, Y.; Midorikawa, K. Attosecond Probing of Vibrational Dynamics with High-Harmonic Generation. *New J. Phys.* **2008**, *10*, 025036.

(12) Chirilă, C. C.; Lein, M. Influence of Nuclear Vibration on Harmonic Generation in Molecules. *J. Phys. B: At. Mol. Opt. Phys.* **2006**, *39*, S437−S444.

(13) Patchkoviskii, S. Nuclear Dynamics in Polyatomic Molecules and High-order Harmonic Generation. *Phys. Rev. Lett.* **2009**, *102*, 253602.

(14) Saenz, A. On the Influence of Vibrational Motion on Strong-Field Ionization Rates in Molecules. *J. Phys. B: At. Mol. Opt. Phys.* **2000**, *33*, 4365−4372.

(15) Goll, E.; Wunner, G.; Saenz, A. Formation of Ground-state Vibrational Wave Packets in Intense Ultrafast Laser Pulses. *Phys. Rev. Lett.* **2006**, *97*, 103003.

(16) Farrell, J. p.; Petretti, S.; Förster, J.; McFarland, B. K.; Spector, L. S.; Vanne, Y. V.; Decleva, P.; Bucksbaum, P. H.; Saenz, A.; Gühr, M. Strong Field Ionization to Multiple Electronic States in Water. *Phys. Rev. Lett.* **2011**, *107*, 083001.

(17) Kraus, P. M.; Wörner, H. J. Attosecond Nuclear Dynamics in the Ammonia Cation: Relation between High-Harmonic and Photoelectron Spectroscopies. *ChemPhysChem* **2013**, *14*, 1445−1450.

(18) Förster, J.; Saenz, A. Theoretical Study of the Inversion Motion of the Ammonia Cation with Subfemtosecond Resolution for High-Harmonic Spectroscopy. *ChemPhysChem* **2013**, *14*, 1438−1444.

(19) Mondal, T.; Varandas, A. J. C. Quadratic Coupling Treatment of the Jahn−Teller Effect in the Triply-Degenerate Electronic State of CH_4^+: Can One Account for Floppiness? *J. Chem. Phys.* **2012**, *137*, 214320.

(20) Mondal, T.; Varandas, A. J. C. Varandas, Silane Radical Cation: A Theoretical Account on the Jahn−Teller Effect at a Triple Degeneracy. *J. Phys. Chem. A* **2013**, *117*, 8794−8805.

(21) (a) Worth, G. A.; Beck, M. H.; Jäckle, A.; Meyer, H.-D. *The MCTDH Package, Version 8.2*; University of Heidelberg: Heidelberg, Germany, 2000. (b) Meyer, H.-D. *The MCTDH Package, Version 8.3*. Available via the Internet at http://www.pci.uni-heidelberg.de/tc/usr/mctdh/, 2002.

(22) Meyer, H.-D.; Manthe, U.; Cederbaum, L. S. The Multiconfigurational Time-Dependent Hartree Approach. *Chem. Phys. Lett.* **1990**, *165*, 73−78.

(23) Manthe, U.; Meyer, H.-D.; Cederbaum, L. S. Wave-Packet Dynamics Within the Multiconfiguration Hartree Framework: General Aspects and Application to NOCl. *J. Chem. Phys.* **1992**, *97*, 3199−3213.

(24) Beck, M. H.; Jäckle, A.; Worth, G. A.; Meyer, H.-D. The Multiconfiguration Time-Dependent Hartree (MCTDH) Method: A Highly Efficient Algorithm for Propagating Wavepackets. *Phys. Rep.* **2000**, *324*, 1−105.

(25) *Multidimensional Quantum Dynamics: MCTDH Theory and Applications*; Meyer, H.-D., Gatti, F., Worth, G. A., Eds.; Wiley−VCH: Weinheim, Germany, 2009; pp 1−446.

(26) Mondal, T.; Varandas, A. J. C. The Jahn−Teller Effect in the Triply Degenerate Electronic State of Methane Radical Cation. *J. Chem. Phys.* **2011**, *135*, 174304.

(27) Jahn, H. A.; Teller, E. Stability of Polyatomic Molecules in Degenerate Electronic States. I. Orbital Degeneracy. *Proc. R. Soc. London, Ser. A* **1937**, *161*, 220−235.

(28) Opik, U.; Pryce, M. H. L. Studies of the Jahn−Teller Effect. I. A Survey of the Static Problem. *Proc. R. Soc. London, Ser. A* **1957**, *238*, 425−447.

(29) Longuet-Higgins, H. C.; Opik, U.; Pryce, M. H. L.; Sack, R. A. Studies of the Jahn−Teller Effect. II. The Dynamical Problem. *Proc. R. Soc. London, Ser. A* **1958**, *244*, 1−16.

(30) Longuet-Higgins, H. C. Some Recent Developments in the Theory of Molecular Energy Levels. *Adv. Spectrosc.* **1961**, *2*, 429−472.

(31) Englman, R. *The Jahn−Teller Effect in Molecules and Crystals*; Wiley: New York, 1972.

(32) Köppel, H.; Domcke, W.; Cederbaum, L. S. Multimode Molecular-Dynamics Beyond the Born-Oppenheimer Approximation. *Adv. Chem. Phys.* **1984**, *57*, 59−246.

(33) Bersuker, I. B. Modern Aspects of the Jahn−Teller Effect Theory and Applications to Molecular Problems. *Chem. Rev.* **2001**, *101*, 1067−1114.

(34) Bersuker, I. B. *The Jahn−Teller Effect*; Cambridge University Press: Cambridge, U.K, 2006; pp 1−632.

(35) Bersuker, I. B.; Polinger, V. Z. The Second Order $T−e−t_2$ Problem in the Jahn−Teller Effect Theory. A New Type of Adiabatic Potential Minima and Inversion (Tunneling) Splitting. *Phys. Lett. A* **1973**, *44*, 495−496.

(36) Bersuker, I. B.; Polinger, V. Z. *Sov. Phys. JETP* **1974**, *39*, 1023.

(37) Ceulemans, A.; Beyens, D.; Vanquickenborne, L. G. Symmetry Aspects of Jahn−Teller Activity: Structure and Reactivity. *J. Am. Chem. Soc.* **1984**, *106*, 5824−5837.

(38) Moffitt, W.; Thorson, W. Vibronic States of Octahedral Complexes. *Phys. Rev.* **1957**, *108*, 1251−1255.

(39) Dunning, T. H., Jr. Gaussian Basis Sets for Use in Correlated Molecular Calculations. I. The Atoms Boron Through Neon and Hydrogen. *J. Chem. Phys.* **1989**, *90*, 1007−1023.

(40) Frisch, M. J.; Trucks, G. W.; Schlegel, H. B.; Scuseria, G. E.; Robb, M. A.; Cheeseman, J. R.; Montgomery, Jr., J. A.; Vreven, T.; Kudin, K. N.; Burant, J. C.; Millam, J. M.; Iyengar, S. S.; Tomasi, J.; Barone, V.; Mennucci, B.; Cossi, M.; Scalmani, G.; Rega, N.; Petersson, G. A.; Nakatsuji, H.; Hada, M.; Ehara, M.; Toyota, K.; Fukuda, R.; Hasegawa, J.; Ishida, M.; Nakajima, T.; Honda, Y.; Kitao, O.; Nakai, H.; Klene, M.; Li, X.; Knox, J. E.; Hratchian, H. P.; Cross, J. B.; Bakken, V.; Adamo, C.; Jaramillo, J.; Gomperts, R.; Stratmann, R. E.; Yazyev, O.; Austin, A. J.; Cammi, R.; Pomelli, C.; Ochterski, J. W.; Ayala, P. Y.; Morokuma, K.; Voth, G. A.; Salvador, P.; Dannenberg, J. J.; Zakrzewski, V. G.; Dapprich, S.; Daniels, A. D.; Strain, M. C.; Farkas, O.; Malick, D. K.; Rabuck, A. D.; Raghavachari, K.; Foresman, J. B.; Ortiz, J. V.; Cui, Q.; Baboul, A. G.; Clifford, S.; Cioslowski, J.; Stefanov, B. B.; Liu, G.; Liashenko, A.; Piskorz, P.; Komaromi, I.; Martin, R. L.; Fox, D. J.; Keith, T.; Al-Laham, M. A.; Peng, C. Y.;

Nanayakkara, A.; Challacombe, M.; Gill, P. M. W.; Johnson, B.; Chen, W.; Wong, M. W.; Gonzalez, C.; and Pople, J. A. *Gaussian 03, Revision C.02*; Gaussian, Inc.: Wallingford, CT, 2004.

(41) *NIST Chemistry Webbook*; Available via the Internet at http://webbook.nist.gov/chemistry, last accessed on July 4, 2014.

(42) Werner, H. J.; Knowles, P. J.; Knizia, G.; Manby, F. R.; Schütz, M.; Celani, P.; Korona, T.; Lindh, R.; Mitrushenkov, A.; Rauhut, G.; Shamasundar, K. R.; Adler, T. B.; Amos, R. D, Bernhardsson, A.; Berning, A.; Cooper, D. L.; Deegan, M. J. O.; Dobbyn, A. J.; Eckert, F.; Goll, E.; Hampel, C.; Hesselmann, A.; Hetzer, G.; Hrenar, T.; Jansen, G.; Köppl, C.; Liu, Y.; Lloyd, A. W.; Mata, R. A.; May, A. J. McNicholas, S. J.; Meyer, W.; Mura, M. E.; Nicklass, A.; O'Neill, D. P.; Palmieri, P.; Pflüger, K.; Pitzer, R.; Reiher, M.; Shiozaki, T.; Stoll, H.; Stone, A. J.; Tarroni, R.; Thorsteinsson, T.; Wang, M.; Wolf, A. *Molpro*, Version 2010.1; A Package of Ab Initio Programs, 2010. Available via the Internet at http://www.molpro.net.

(43) Levenberg, K. Q. *Appl. Math.* **1944**, *2*, 164−168.

(44) Marquardt, D. W. An Algorithm for Least-Squares Estimation of Nonlinear Parameters. *SIAM J. Appl. Math.* **1963**, *11*, 431−441.

(45) Wigner, E. P. On the Behavior of Cross Sections Near Thresholds. *Phys. Rev.* **1948**, *73*, 1002−1009.

(46) Domcke, W.; Köppel, H.; Cederbaum, L. S. Spectroscopic Effects of Conical Intersections of Molecular Potential Energy Surfaces. *Mol. Phys.* **1981**, *43*, 851−875.

(47) Potts, A. W.; Price, W. C. The Photoelectron Spectra of Methane, Silane, Germane and Stannane. *Proc. R. Soc. London Ser. A* **1972**, *326*, 165−179.

(48) Cullum, J.; Willoughby, R. *Lanczos Algorithms for Large Symmetric Eigenvalue Problems*, Vols. I and II; Birkhäuser: Boston, 1985.

(49) Mairesse, Y.; de Bohan, A.; Frasinski, L. J.; Merdji, H.; Dinu, L. C.; Monchicourt, P.; Breger, P.; Kovacev, M.; Taïeb, R.; Carre, B.; Miller, H. G.; Agostini, P.; Salieres, P. Attosecond Synchronization of High-Harmonic Soft X-rays. *Science* **2003**, *302*, 1540−1543.

(50) Urbain, X.; Fabre, B.; Staicu-Casagrande, E. M.; de Ruette, N.; Andrianarijaona, V. M.; Jureta, J.; Posthumus, J. H.; Saenz, A.; Baldit, E.; Cornaggia, C. Intense-Laser-Field Ionization of Molecular Hydrogen in the Tunneling Regime and Its Effect on the Vibrational Excitation of H_2^+. *Phys. Rev. Lett.* **2004**, *92*, 163004.

(51) Frey, R. F.; Davidson, E. R. Potential Energy Surfaces of CH_4^+. *J. Chem. Phys.* **1988**, *88*, 1775−1785.

(52) Knight, L. B., Jr.; Steadman, J.; Feller, D.; Davidson, E. R. Experimental Evidence For a $C_{2v}(^2B_1)$ Ground-State Structure of the Methane Cation Radical: ESR and Ab Initio CI Investigations of Methane Cation Radicals (CH_4^+ and $CD_2H_2^+$) in Neon Matrixes at 4 K. *J. Am. Chem. Soc.* **1984**, *106*, 3700−3701.

(53) Vager, Z.; Kanter, E. P.; Both, G.; Cooney, P. J.; Faibis, A.; Koenig, W.; Zabransky, B. J.; Zajfman, D. Direct Determination of the Stereochemical Structure of CH_4^+. *Phys. Rev. Lett.* **1986**, *57*, 2793−2795.

(54) Paul, P. M.; Clatterbuck, T. O.; Lyngå, C.; Coloslmo, P.; DiMauro, L. F.; Agostini, P.; Kulander, K. C. Enhanced High Harmonic Generation from an Optically Prepared Excited Medium. *Phys. Rev. Lett.* **2005**, *94*, 113906.